Research Square

Preprints are preliminary reports that have not undergone peer review.
They should not be considered conclusive, used to inform clinical practice,
or referenced by the media as validated information.

West Antarctic Ice Sheet collapse and North Atlantic meltwater reconcile Last Interglacial climate records

Joseph Schnaubelt

joseph.schnaubelt@uconn.edu

University of Connecticut https://orcid.org/0000-0003-0561-9104

Clay Tabor

University of Connecticut https://orcid.org/0000-0002-9915-6157

Ran Feng

University of Connecticut https://orcid.org/0000-0002-4433-4745

Austin Carter

Princeton University https://orcid.org/0000-0001-5153-2507

Sarah Aarons

Columbia University

Johannes Sutter

Climate and Environmental Physics, Physics Institute, and Oeschger Centre for Climate Change Research, University of Bern, Bern, Switzerland https://orcid.org/0000-0002-3357-2633

Nicholas Golledge

Victoria University of Wellington https://orcid.org/0000-0001-7676-8970

Eric Steig

University of Washington https://orcid.org/0000-0002-8191-5549

Article

Keywords:

Posted Date: July 21st, 2026

DOI: https://doi.org/10.21203/rs.3.rs-10348076/v1

License: This work is licensed under a Creative Commons Attribution 4.0 International License.
Read Full License

Additional Declarations: There is **NO** Competing Interest.

West Antarctic Ice Sheet collapse and North Atlantic meltwater reconcile Last Interglacial climate records

Joseph Schnaubelt[1*], Clay Tabor[1], Ran Feng[1], Austin Carter[2], Sarah Aarons[3], Johannes Sutter[4], Nicholas Golledge[5], Eric J. Steig[6]

[1]Department of Earth Sciences, University of Connecticut, Storrs, CT, USA.

[2]Department of Geosciences, Princeton University, Princeton, NJ, USA.

[3]Department of Earth and Environmental Sciences, Columbia University, New York, NY, USA.

[4]Climate and Environmental Physics, Physics Institute, University of Bern, Bern, Switzerland.

[5]Antarctic Research Centre, Victoria University of Wellington, Wellington, New Zealand.

[6]Department of Earth and Space Sciences, University of Washington, Seattle, WA, USA.

[*]Corresponding author. Email: joseph.schnaubelt@uconn.edu

The Last Interglacial (LIG; 131,000-118,000 years ago) had a global mean sea level that was approximately 5-10 m above preindustrial levels. This requires substantial melt contributions from both the Greenland and Antarctic ice sheets, yet the partitioning of this melt remains unclear. Here, we use an ensemble of water isotope enabled Earth system model simulations with variable Antarctic ice sheet and glacial meltwater flux configurations to characterize the regional climate response to a substantially reduced ice sheet, and glacial meltwater in the North Atlantic and/or Southern Ocean. We compare our simulations with southern high latitude records to constrain the paleo-environmental drivers of anomalous signals in Antarctic ice and Southern Ocean sediments dating to the LIG. Our results suggest that a reduced West Antarctic Ice Sheet, and the release

of glacial meltwater into the North Atlantic following Heinrich Event 11 (~135,000-130,000 years ago), are together responsible for highly isotopically enriched $\delta^{18}O$ values in Antarctic ice, warm Southern Ocean temperatures, and reduced sea ice concentrations during the LIG. This indicates that the Antarctic ice sheet may have been highly vulnerable to ocean warming in the past, with a demonstrated potential to contribute up to ~4 m to global mean sea level.

1 Introduction

The Last Interglacial (LIG; 131,000-118,000 years ago) featured a more eccentric orbit than present day and, early in the LIG, perihelion during the boreal summer delivered ~16% more insolation during the month of June to the high Northern latitudes (65°N). This drove intense high latitude warmth and triggered multiple Earth system feedbacks such as reduced seasonal sea ice in both hemispheres (*1–4*), poleward expansion of boreal forest (*5*), greening of the Sahara (*6*), and significant changes in oceanic and atmospheric circulation (*7*). Crucially, global mean sea level (GMSL) during the LIG was likely 5 to 10 m higher than present day (*8, 9*). While the drivers of LIG climate change differ from those of the present, the relative recency and abundance of proxy records make it a powerful benchmark for isolating the drivers of large scale sea level rise.

Such a significant increase in GMSL requires contributions from the polar ice sheets, with smaller contributions coming from ocean steric expansion ($< 0.4 \pm 0.3$ m) (*10*) and mountain glacier retreat ($< 0.2 \pm 0.1$ m) (*11*). The Greenland Ice Sheet (GrIS) may have contributed up to 2 m of sea level rise during the LIG (*12*). The remaining sea level likely came from retreat of the Antarctic Ice Sheet (AIS). Partitioning the contributions from each ice sheet is further complicated by the fact that retreat may have been asynchronous during the LIG (*9, 13–15*).

Geological records throughout the Southern Ocean and within Antarctica provide evidence for a substantially reduced AIS during the LIG. Marine diatoms in sediments found beneath the West Antarctic Ice Sheet (WAIS) suggest collapse during the late Pleistocene (*16*), with recent genomic evidence indicating an open ocean gateway during the LIG, suggesting a complete collapse of the WAIS (*17*). Similarly, offshore sediments of LIG age from the Bellinghausen Sea show a lack of WAIS-derived material, indicating regional grounding line retreat (*18*). Ice recovered from the

Patriot Hills has a hiatus during the warmest interval of the LIG, which is preceded by highly enriched water isotope ratios (*19*). This could reflect a retreat of the WAIS during that period, or dynamical thinning and a shift in ice flow.

Ice-sheet modeling can be used to evaluate the response of past ice sheets to static and transient forcings. Past work has shown that the long suppression of the Atlantic Meridional Overturning Circulation during and following Heinrich Event 11 (H11) should have led to significant AIS retreat and suppressed GrIS retreat (*15*). One recent study found that an ice sheet simulation which resulted in collapse of the Amundsen Sea sector and thinning around the remainder of the WAIS and coastal East Antarctic Ice Sheet could explain the majority of the above geological records and sea-level reconstructions during the LIG (*20*). This WAIS retreat scenario would account for ~4 m of sea level equivalent melt from the Antarctic ice sheet aligning with estimates for the LIG sea-level highstand if the GrIS, mountain glaciers, and thermosteric expansion contributed ≥1 m. Other ice-sheet models suggest a much more substantial retreat of the AIS during the LIG (*21, 22*). These differences stem from varying parameterizations, including ice-cliff and ice-shelf instabilities, and uncertain ocean temperature thresholds for WAIS collapse. While central to future sea-level rise projections, these factors remain highly uncertain; some studies find Southern Ocean warming thresholds of 2–3°C (*21, 22*) sufficient for collapse, whereas others suggest thresholds as low as 0–0.25°C (*23, 24*).

Despite the evidence for a reduced WAIS during the LIG, the configuration and magnitude of retreat remains unknown. To this end, we explore the application of ice core records to constraining WAIS loss scenarios. Ratios of stable water isotopes of precipitation, $\delta^{18}O_p$ and δD_p, preserved in ice cores, record changes in temperature and atmosphere circulation. Water isotopes in Antarctic ice (e.g. $\delta^{18}O_{ice}$) should record large shifts in regional hydroclimate associated with a decrease in ice-sheet topography and regional ocean surface conditions. Most East Antarctic ice cores dating to the LIG record an enrichment in $\delta^{18}O_{ice}$ spanning 2-5‰ above late Holocene and 1-3‰ above early Holocene values (*25, 26*). This enrichment could be related to an increase in regional temperatures or shifts in moisture transport, both of which would result from a collapse of the WAIS (*26, 27*). Alternatively, this enrichment could be due to increased Southern Ocean temperatures, reduced seasonal sea ice coverage, and closer vapor sources to the AIS, and thus reduced Rayleigh distillation from evaporation to precipitation over the ice sheet, without necessarily involving a change in

ice-sheet elevation (*28*). Indeed, glacial meltwater released into the North Atlantic drove warm Southern Ocean temperatures following Heinrich Event 11 (*29*), which likely reduced seasonal sea ice coverage, suggesting that at least some signal from warm Southern Ocean temperatures is recorded in Antarctic ice cores. The combination of AIS topography, Southern Ocean temperatures, and sea-ice coverage recorded in Antarctic ice provides essential information about the sensitivity of Antarctica to future ocean warming and the risk of future sea level rise.

The sensitivity of regional Antarctic climate to WAIS collapse and freshwater hosing has been explored in several previous studies. Climate model simulations testing the sensitivity of regional climate to WAIS collapse have shown patterns of warming broadly consistent with reductions in elevation, but with some locations experiencing cooling due to cyclonic circulation anomalies (*26, 30*). This pattern has been reproduced in other models and has been shown to be robust to the addition of glacial meltwater to the Southern Ocean (*31*). Similarly, recent work has shown that Antarctic $\delta^{18}O_{ice}$ is better reproduced in model simulations when some reduction of the AIS is included (*32*). Other models have successfully reproduced the magnitude of Antarctic $\delta^{18}O_{ice}$ only with the addition of Heinrich-like meltwater in the North Atlantic and a significant retreat of Southern Ocean sea ice coverage (*28, 33*). Southern Ocean warming induced by North Atlantic hosing has also been shown to be essential for reproducing Southern Ocean sea surface temperatures and sea ice concentrations inferred from proxy data dating to the LIG (*34, 35*).

To provide new constraints on the configuration of the Antarctic ice sheet during the LIG, we performed a suite of fully coupled climate model simulations using the water isotope enabled version of the Community Earth System Model (iCESM) (*36*). These simulations include four different realistic AIS topographies, and both North Atlantic and Southern Ocean glacial meltwater scenarios, allowing us to evaluate the response of Antarctic and Southern Ocean climate under a comprehensive range of forcings. We compare our simulations with eight Antarctic ice core $\delta^{18}O_{ice}$ records, and a compilation of Southern Ocean summertime sea surface temperatures (SST_{djf}) (*34, 37*) and September sea ice concentrations (SICs) (*3*) to evaluate which boundary conditions best reproduce Antarctic and Southern Ocean climate during the LIG. Additionally, we employ passive water tracers in iCESM to determine the mechanisms of enriched $\delta^{18}O_p$ values due to a collapse of the WAIS.

2 Results

2.1 Antarctic topographic reconstructions

We use four separate configurations of the Antarctic ice sheet for our LIG simulations (*LIG*, *LIG_noASE*, *LIG_noShelves*, and *LIG_collapsed*) (Fig. 1), based on ice-sheet model simulations providing spatially consistent and plausible WAIS collapse scenarios. A preindustrial (PI) configuration, based on Bedmap2 Antarctic topography (*38*), serves as a baseline ice sheet configuration with no sea level equivalent (SLE) ice mass loss. A *LIG_noShelves* configuration, in which the Ross and Filchner-Ronne ice shelves are removed (*39*), and a *LIG_noASE* configuration, in which much of the ice in the Amundsen Sea Embayment (ASE) is removed (*20*), are consistent with ~4 m and ~2 m of SLE AIS mass loss respectively. Finally a *LIG_collapsed* configuration, which removes both major ice shelves and has additional interior collapse of the WAIS resulting in an open ocean gateway (*39*), is consistent with ~4 m of SLE AIS mass loss.

2.2 Upper ocean response to hosing and Antarctic ice sheet retreat

Increased North Atlantic freshwater flux (NAFWF) or hosing drives a significant weakening of the AMOC (Fig. 2b,d) decreasing the transport and ventilation of heat in the North Atlantic (*15, 35, 40*). There is minimal change in AMOC strength without the inclusion of glacial meltwater (Fig. 2a,c). To compare the impact of AIS topography and freshwater hosing on ocean heat transport, we calculate the magnitude of ocean heat transport with $|OHT| = c_p \rho \int \overline{v} T dz$ where c_p is the heat capacity of seawater, ρ is the average density of seawater, and $\overline{v}$, and T are the flow vector and temperature, respectively. Weakened northward heat transport in the Atlantic cools surface conditions in the North Atlantic and accumulates heat in the Southern Ocean, which then ventilates and raises surface temperatures (*41*) (Fig. 2h,j,k). Higher Southern Ocean temperatures melt sea ice, decrease albedo, and drive further Southern Ocean warming through ice-albedo feedbacks (Fig. 2l,n). Collapse of the WAIS drives Southern Ocean warming even without North Atlantic hosing (Fig. 2i) (*26, 42*). Removing portions of the WAIS exposes the upper ocean to increased shortwave radiation, allows ocean heat transport into new regions, warming the surface, driving sea ice melt, and further warming (Fig. 2m). Additional ocean surface warming occurs due to an increase in

southward atmospheric energy transport, and a shift in ocean circulation patterns (*31, 42, 43*). This heating is mostly localized around the portions of the WAIS which are removed but is then circulated throughout the Southern Ocean by the Antarctic Circumpolar Current (Fig. 2h). Southern Ocean hosing (SOFWF) drives a slight weakening of AMOC (Fig. 2e) and a similar increase in top-of-atmosphere radiative imbalance where the ice sheet collapses (Fig. 2o). However, the expansion of sea ice and increased buoyancy of surface waters keeps heat from ventilating and warming the surface ocean, but accumulates heat in the subsurface Southern Ocean (Fig. 2j).

Southern Ocean summertime SSTs increase by ~1°C with local cooling occurring north of ~50°S due to LIG orbital and greenhouse gas conditions (Fig. 3a). The inclusion of north Atlantic hosing drives an additional warming of 1-2°C over the entire Southern Ocean even without reducing ice sheet topography (Fig. 3b). WAIS collapse warms the Southern Ocean south of ~50°S (Fig. 3c). The combined impact of increased radiative forcing on the upper ocean and heat accumulation drive the warmest Southern Ocean temperatures in the *LIG_collapsed_NAFWF* simulation (Fig. 3d).

September SICs decrease broadly in line with summertime SST increase with the default *LIG* simulation showing little change from *PI*, but the *LIG_NAFWF*, *LIG_collapsed*, and *LIG_collapsed_NAFWF* experiencing substantial retreat, especially in the Atlantic sector (Fig. 3g,h,i). The *LIG_collapsed* simulation experiences broader $SIC_{Sept.}$ decrease than the *LIG_NAFWF* simulation due to stronger SST warming close to the AIS, increased sea ice coverage in the Ross and Weddell Seas, and a reduced latitudinal expansion of sea ice coverage. SICs decrease further in the *LIG_collapsed_NAFWF* simulation, but the pattern of loss matches the *LIG_collapsed* simulation, suggesting that ice sheet configuration plays a dominant role in controlling the pattern of sea ice retreat. The addition of freshwater hosing throughout the Southern Ocean (SOFWF) cools summertime SSTs and expands September SICs in the *LIG_collapsed_SOFWF* simulation (Fig. 3f,k), but the combined impact of freshwater hosing in the North Atlantic and Southern Ocean in the *LIG_collapsed_NAFWF_SOFWF* simulation favors some warming and sea ice retreat across the Southern Ocean (Fig. 3e,j). Similar patterns of SST increase and sea ice retreat exist in all ice sheet collapse simulations but the *LIG_collapsed_NAFWF* simulation has the strongest signal (Fig. S1).

2.3 Atmospheric response to ice sheet collapse

Surface temperatures over Antarctica increase uniformly by ~1°C during the LIG due to orbital configuration and greenhouse gas concentrations (Fig. 4a). Changing ice sheet topography, however, results in heterogeneous changes in surface temperature. Surface temperatures are inversely dependent on elevation change in each Antarctic collapse scenario. Each simulation with a reduced AIS cools by 0-2°C near the South Pole, where elevation increases in each simulation. Up to 4°C warming across East Antarctica is observed due to changes in local elevation and regional circulation. Some cooling is also simulated around the East Antarctic coastline due to slight variations in ice sheet extent in our ice sheet reconstructions. West Antarctica warms by up to 6°C across stable portions of the ice sheet and ≥10°C where ice is replaced by open ocean (Fig. 4e,i,m).

Surface temperatures and changes in ice sheet topography drive changes in precipitation around Antarctica. A minimal change in precipitation is observed with a PI-like ice sheet during the LIG (Fig. 4b), but a reduced WAIS brings more moisture over West Antarctica and peripheral East Antarctica as previous work has emphasized (*26, 30*). As with surface temperature, regions of the ice sheet where elevation is decreased see more precipitation, especially near coastal areas (Fig. 4f,j,n). Some regions of the Southern Ocean experience less precipitation due to enhanced poleward moisture advection over the ice sheet decreasing the moisture budget in these regions. Increased precipitation rates of up to ~1 mm/day occur across the Ross and Weddell Seas close to the Antarctic margin in the *LIG_noShelves* and *LIG_collapsed* simulations due to open ocean and the lack of ice shelves at these locations. Similarly, the *LIG_noASE* and *LIG_collapsed* simulations see up to 1 mm/day increase in precipitation rates near the Amundsen Sea Embayment and Marie Byrd Land.

Changes in temperature and precipitation closely correlate with changes in the isotopic composition of water vapor ($\delta^{18}O_v$) and precipitation ($\delta^{18}O_p$) over the ice sheet. An enrichment in $\delta^{18}O_v$ (≤3‰) occurs homogeneously over Antarctica during the LIG with a PI-like AIS (Fig. 4c). The collapse of WAIS significantly alters this pattern, resulting in an enrichment of up to ~7‰ in $\delta^{18}O_v$ values in West Antarctica, centered around regions with the greatest topographic reduction, and an enrichment of up to ~5‰ across East Antarctica. This excludes areas that increase in elevation, such as near the South Pole, where $\delta^{18}O_v$ values are depleted by ~-1-4‰ (Fig. 4g,k,o).

As ice sheet elevation is decreased the air column is stretched and relative vorticity must increase to conserve potential vorticity in barotropic flow, thus inducing a cyclonic anomaly, and strengthening easterly winds around the ice sheet coastline (*26, 44*). These winds in turn increase onshore moisture advection around coastal East Antarctic and the Weddell Sea, and offshore winds towards the Amundsen Sea and parts of the Ross Sea (Fig. 4c). The easterlies strengthen further with reduced AIS topography, but specific wind anomalies depend on ice sheet configuration. Strong onshore winds from the Weddell Sea and offshore winds towards the Ross Sea occur in all three simulations, but especially in the *LIG_noASE* and *LIG_collapsed* simulations (Fig. S2-3). There are also strong onshore wind anomalies over East Antarctica in all three reduced ice sheet simulations (Fig. 4g,k,o). Isotopically enriched vapor ($\delta^{18}O_v$) transported to the Antarctic interior enriches $\delta^{18}O_p$ in all simulations. The relationship between $\delta^{18}O_v$ and $\delta^{18}O_p$ is similar across simulations, suggesting that the supply of isotopically enriched vapor exerts a dominant control of $\delta^{18}O_p$ even in the context of a large change in boundary conditions.

2.4 Atmospheric response to meltwater input

We use North Atlantic and Southern Ocean hosing experiments for each ice sheet configuration to evaluate the impact of Heinrich Event 11 meltwater or Antarctic meltwater on Antarctic water isotopes and Southern Ocean surface conditions. North Atlantic hosing increases surface temperatures over Antarctica by up to ~3°C in the *LIG_collapsed* simulation (Fig. 5a,b). Precipitation increases by ≥1 mm/day over West Antarctica and up to 0.5 mm/day over coastal East Antarctica due to North Atlantic hosing in the *LIG_collapsed* simulation (Fig. 5b,f). A similar change is also observed in the *LIG_noASE* and *LIG_noShelves* simulations with North Atlantic hosing, but the *LIG_collapsed* increase is the largest (Fig. S4, S5). Here, warm temperatures and shifts in moisture transport enrich $\delta^{18}O_v$ by up to 5‰ over East Antarctica and up to 7‰ over West Antarctica. The larger enrichment over West Antarctica reflects the greater changes in elevation there, especially in the *LIG_collapsed* simulation. Onshore winds from the Weddell Sea and offshore winds towards the Ross Sea induced by WAIS collapse are further strengthened with the inclusion of NAFWF.

Southern Ocean hosing has the opposite impacts: surface temperatures cool by up to $5°C$, precipitation decreases over the entire ice sheet (excluding the interior WAIS), $\delta^{18}O_v$ is depleted

by 5‰ near the South Pole and coastal East Antarctica, easterly winds weaken, together depleting $\delta^{18}O_p$ over East Antarctica compared to the *LIG_collapsed* simulation with and without NAFWF (Fig. 5i,j,k,l). The pattern of $\delta^{18}O_p$ enrichment in the *LIG_collapsed_SOFWF* simulation closely matches the pattern in *LIG_collapsed* implying that the $\delta^{18}O_p$ signal is dominated by topographic change. The *LIG_collapsed_NAFWF_SOFWF* simulation, which features simultaneous North Atlantic and Southern Ocean meltwater, displays similar patterns of warming and precipitation to the *LIG_collapsed* simulation, but similar patterns of $\delta^{18}O_v$ and $\delta^{18}O_p$ enrichment and regional winds to the *LIG_collapsed_NAFWF* simulation (Fig. 5m,n,o,p). This suggests that the meltwater resulting from WAIS collapse due to warm Southern Ocean temperatures following a Heinrich event might counteract some of the ice-sheet surface warming and precipitation, but does not strongly influence $\delta^{18}O_p$. Thus, $\delta^{18}O_p$ is primarily a signature of the changed ice sheet topography, with a secondary influence from NAFWF through its impact on Southern Ocean surface warming.

2.5 Reproducing Last Interglacial $\delta^{18}O$ and ocean surface conditions

To constrain the configuration of the Antarctic Ice Sheet during the LIG we compare modeled $\delta^{18}O_p$ to measured $\delta^{18}O_{ice}$ in the compiled ice core records. We assess the accuracy of each simulation as the case that minimizes the mean squared error (MSE) and bias (b) between modeled and measured $\delta^{18}O$ in all ice cores (Methods).

The eight best performing simulations all have some topographic reduction of the WAIS. MSE and bias are minimized with a fully collapsed WAIS and NAFWF (MSE = 0.8‰^{2}; bias=0.1‰^{2}) (*LIG_collapsed_NAFWF*) (Fig. 6a). The *LIG_collapsed_NAFWF_SOFWF* simulation reproduces $\delta^{18}O_{ice}$ nearly as well, suggesting that the best fit scenario is robust to the addition of Southern Ocean freshwater resulting from WAIS collapse, and that Southern Ocean warming following North Atlantic freshwater is a stronger contributor to Antarctic $\delta^{18}O_{ice}$ than cooling after Southern Ocean freshwater when they are synchronous. The *LIG_noASE_NAFWF* and *LIG_noShelves_NAFWF* simulations are the third and fourth best configurations for reducing MSE, suggesting that North Atlantic hosing and reduced ice elevation are both essential features of the Antarctic isotope record during the LIG. Simulations with PI-like topography or with the inclusion of Southern Ocean hosing in isolation do not reproduce $\delta^{18}O_{ice}$ well. Many of the most accurate simulations (*LIG_collapsed_NAFWF*,

LIG_collapsed_NAFWF_SOFWF, *LIG_noASE_NAFWF*, *LIG_noShelves_NAFWF*) favorably reproduce West Antarctic ice cores (Mount Moulton and Skytrain), even without North Atlantic hosing. Crucially, these locations are the most sensitive to large changes in ice sheet topography and their mutual agreement suggests a shared sensitivity to topographically induced changes in circulation (*26, 30*).

We also compare our simulations to several compilations of proxy-recorded summertime SSTs (*1, 37, 45*) and September SICs (*3*) (Fig. 6b). In this case, MSE and bias for Summertime SSTs are minimized in the *LIG_noShelves_NAFWF* (MSE=3.9°C^2; bias=0.1°C^2) simulation. However, the next four simulations perform nearly as well with MSE spanning from 3.9-4.9°C^2 and bias from 0.1-1.2°C^2). September SICs do not favor a particular simulation when considering MSE, but the bias is significantly reduced in *LIG_collapsed_NAFWF*, *LIG_collapsed_NAFWF_SOFWF*, *LIG_noASE_NAFWF*, and *LIG_noShelves_NAFWF*. This reflects model skill in producing the magnitude of September SICs decrease across the Southern Ocean but a lack of skill in distinguishing among possible patterns of retreat captured by the proxy records. Each of these simulations use North Atlantic hosing, highlighting its role in driving Southern Ocean warmth during the LIG as observed in other modeling studies (*33, 35*). The simulations that only include Southern Ocean hosing fail to reproduce summertime SSTs or SICs, suggesting that any melt from the WAIS did not have a significant impact on Southern Ocean surface conditions recorded in proxy records.

We note that different model configurations best reproduce Antarctic surface $\delta^{18}O_{ice}$ and Southern Ocean SSTs and SICs during the LIG. However, the relative improvement in performance associated with topography for surface $\delta^{18}O_{ice}$ is larger than that for SSTs and SICs. The total error in comparing SST_{djf} and September SICs is primarily variance while the error in comparing $\delta^{18}O$ is largely composed of bias. We interpret this to reflect a homogeneous impact on $\delta^{18}O_p$ across the AIS due to WAIS collapse and hosing while a comparatively heterogeneous pattern of SST_{djf} warming and September SICs retreat increase variance in those variables. Furthermore, we note that the better overall performance of *LIG_noASE_NAFWF* compared with *LIG_noShelves_NAFWF* is consistent with the finding, based on sea-salt concentrations in the Skytrain ice core, that the Ronne ice shelf likely survived the LIG (*46*).

2.6 Decomposing $\delta^{18}O$ response to WAIS collapse and hosing

We observe a depletion in $\delta^{18}O_{v,source}$ in all LIG simulations compared to the PI simulation (Fig. 7a,b,c,d,e). This depletion is strongest in the *LIG_collapsed_SOFWF* and weakest in the *LIG_collapsed_NAFWF* simulations suggesting Southern Ocean temperature plays a strong control. However, the dominant driver of $\delta^{18}O$ change is rainout ($\Delta(\delta^{18}O_{v,AIS} - \delta^{18}O_{v,source})$), or the preferential precipitation of heavy isotopes as moisture moves from source to the AIS (Fig. 7f,g,h,i,j). This accounts for the majority of the $\delta^{18}O_p$ signal over West and East Antarctica and is related to more proximal moisture sources owing to warmer high latitude temperatures and the collapse of the WAIS removing a topographic barrier. The rainout signal includes depletion in $\delta^{18}O_{v,source}$ that might result from more southward vapor sources, but the southward shift of moisture source suggests a large enrichment signal due to decreased precipitation of heavy isotopologues along moisture trajectories (Fig. 7p,q,r,s,t). Isotopic enrichment from rainout increases due to both WAIS collapse and NAFWF. Small southward shifts in average moisture source latitude occur in all simulations but especially the *LIG_collapsed* and *LIG_collapsed_NAFWF* simulations where the warmest Southern Ocean temperatures occur. Condensation changes ($\Delta(\delta^{18}O_{p,AIS} - \delta^{18}O_{v,AIS})$) deplete $\delta^{18}O_p$ over Victoria Land, Dronning Maud Land, and parts of West Antarctica, and enrich $\delta^{18}O_p$ along the East Antarctic coastline and near the South Pole (Fig. 7p,q,r,s,t). The exact drivers of this pattern are likely related to varying patterns of temperature change and katabatic flow (*43*). Changes in $\delta^{18}O_p$ caused by condensation are much smaller than those caused by rainout, once again highlighting the dominant control of vapor supply on $\delta^{18}O_p$.

We also evaluate the sensitivity of Antarctic $\delta^{18}O_p$ signatures to changes in seasonal precipitation by switching the distribution of seasonal precipitation between LIG and PI states (methods). Using PI monthly precipitation distributions but LIG $\delta^{18}O_p$, we find that the annually averaged precipitation weighted $\delta^{18}O_p$ retains most of the LIG signature. Alternatively, using PI $\delta^{18}O_p$ but the LIG seasonal distribution of precipitation minimal change is observed (Fig. S6). This highlights that the influence of changes in the seasonal distribution of precipitation on Antarctic $\delta^{18}O_p$ is small compared to the signal imparted by a change in moisture source, circulation, or regional temperatures.

3 Discussion

Collapse of the WAIS induces ocean surface warming related to ice-albedo feedbacks and changes in regional circulation associated with the loss of large ice shelves. Much of this warming is localized close to the AIS but large scale Southern Ocean warming of sufficient magnitude to compare well with independent proxy data is achieved only with the inclusion of NAFWF, as seen in other models of the LIG (*28, 34, 35*). Both drivers of Southern Ocean warming reduce sea ice coverage and bring the maximum sea ice edge closer to the AIS, but the collapse-induced warming drives a larger southward retreat of the September sea ice edge. This is related to stronger albedo-induced warming near the Lazarev, Riiser-Larsen, and Cosmonaut Seas in the collapsed simulations. Southern Ocean surface warming occurs even when Southern Ocean glacial meltwater is included (*LIG_collapsed_NAFWF_SOFWF*), suggesting that elevated Southern Ocean temperatures due to reduced AMOC probably persisted even after WAIS collapse.

Previous interpretations of Antarctic ice core isotope records suggest 0.9-3.3°C of warming over East Antarctica during the LIG (*25, 35*). Our simulations that include a reduced AIS and/or NAFWF reproduce this magnitude of warming, suggesting that at least one of those features is necessary for explaining the anomalous isotopic enrichment early in the LIG. We show that large changes in elevation may result in more modest changes in temperature than expected based on lapse rate relationships. This is related to changes in regional circulation which may have important implications for ice core interpretations (*47*). A reduction of the AIS and Southern Ocean warming due to glacial meltwater in the North Atlantic results in large increases in precipitation over the ice sheet. This manifests as an increase in accumulation rate which is recorded in the blue ice from the Allan Hills, East Antarctica and is replicated in climate simulations when the Ross Ice Shelf is removed (*48, 49*).

Tracking moisture from evaporation to precipitation allows us to identify limited rainout of heavy isotopes as the dominant driver of $\delta^{18}O_p$ enrichment at the LIG. Both NAFWF and WAIS collapse warm the Southern Ocean sufficiently to generate more locally sourced moisture, but only WAIS collapse removes the topographic barrier allowing more efficient advection of moisture further inland. Shifts in moisture transport, such as those brought about by WAIS collapse and regional freshwater release, may introduce nonlinear relationships between $\delta^{18}O_p$, elevation, and

surface temperature that complicate our interpretation of $\delta^{18}O_{ice}$ records in ice cores (*26, 47, 50*).

Our simulations along with a compilation of Antarctic ice core $\delta^{18}O_{ice}$, and Southern Ocean SST_{djf} and September SICs, show that AIS collapse and glacial meltwater in the North Atlantic are both necessary to explain the isotopic enrichment, Southern Ocean summertime SST increase, and Southern Ocean sea ice reduction observed during the LIG. The *LIG_collapsed_NAFWF* simulation best reproduces observed $\delta^{18}O_{ice}$ enrichment, SST_{djf} warming, and September SICs retreat.

This study is comprehensive with the inclusion of four different possible AIS configurations, and Southern Ocean, North Atlantic, and simultaneous freshwater hosing scenarios. In the context of transient climate evolution, our results show that Southern Ocean warming resulting from the vast release of freshwater into the North Atlantic following Heinrich Event 11 (*29*) drove warm Southern Ocean temperatures early in the LIG. The warm Southern Ocean may have forced melt of the marine grounded portions of the WAIS (*15*). The ensuing glacial melt may have stratified the surface ocean, driving subsurface warming which could have accelerated ice sheet retreat (*31*), ultimately resulting in a fully collapsed WAIS contributing up to ~4 m to global sea level rise.

Modeling studies have found Southern Ocean warming thresholds for WAIS collapse spanning from 0.25°C to 3°C above preindustrial (*21, 23, 24*), but these estimates do not capture ice-ocean interactions that may be essential for simulating ice sheet evolution. Southern Ocean subsurface (400-500 m) warming of ~0.2-0.6°C (Fig. S7) occurs near the AIS due to LIG orbital configuration and greenhouse gas concentrations alone (Fig. S7a). A reduction of the AIS leads to further warming through wind-driven changes, as has been noted previously (*26, 42, 51*). While NAFWF is crucial for reproducing the magnitude of LIG surface warmth (Fig. 6), it initially cools the subsurface ocean (Fig. S7b,d,h,k). This cooling is transient, giving way to subsurface warming in longer LIG simulations (*33, 40*).

The timing of NAFWF in our simulations (at 127 ka) is idealized. Antarctic mass loss was probably initiated before 127 ka (*20*), and prior work has found a net subsurface warming when NAFWF is applied earlier in the deglaciation, coincident with the timing of H11 (*15*). Nevertheless, our results show that NAFWF is not the only cause of the subsurface warming, which suggests that it may not be necessary for WAIS retreat to be initiated. Regardless, the ensuing meltwater from initial AIS retreat (Fig. S7e,f,i,l) amplifies any subsurface warming, increasing the potential for an ocean-forced collapse. Crucially, one of the simulations with the best overall proxy agreement,

LIG_collapsed_NAFWF_SOFWF, also shows the most subsurface Southern Ocean warming.

Taken together with our proxy comparison, our results suggest that Antarctic melt, initiated by Southern Ocean warming, further amplified subsurface warming to trigger WAIS collapse. The combined impact of forcing (NAFWF, orbital parameters, CO_2) and local feedbacks (lowered ice topography, meltwater), resulted in warmer Southern Ocean surface temperatures, reduced sea ice coverage, and enriched Antarctic water isotopic ratios. The global ocean is already ~0.88°C warmer than the preindustrial and, while the Southern Ocean surface is warming at only ~0.02°C/decade, the subsurface is warming at ~0.1-0.2°C/decade (*8, 52*). Given continued warming, this suggests that the conditions that lead to significant ice sheet retreat may already be present.

4 Methods

4.1 Earth system model

These experiments use the water-isotope enabled version of the Community Earth System Model (iCESM) (*36*). This model uses the fifth version of the Community Atmosphere Model (CAM5), the second version of the Parallel Ocean Protocol (POP2), the fourth version of the Community Land Model (CLM4), the fourth version of the Community Ice CodE (CICE4), and the River Transport Model (RTM). The model is run at a nominal 2-degree horizontal resolution in the land and atmospheric components and 1-degree horizontal resolution in the ocean and sea ice component. The ocean features 60 levels in the vertical and the atmosphere 30 levels in the vertical.

The model is configured with *piControl* or *lig127ka* orbital and greenhouse gas configurations recommended by the Paleoclimate Model Intercomparison Project version 4 (PMIP4) (*53*). This includes greenhouse gas concentrations of CO_2=275 ppm, CH_4=808.2 ppb, and NO_2=255 ppb and orbital eccentricity=0.039378, obliquity=24.040°, and perihelion - 180=275.41. The PI and LIG simulations use the same *noAnthro* potential vegetation where crop and urban land surface types are removed and replaced with the next most dominant plant functional type at that grid cell.

4.2 Ice sheet collapse experiments

Given the elevated sea level at the LIG, we run several experiments with a reduced Antarctic ice sheet. We use three different modeled ice sheet configurations for the LIG from (*39*) and (*20*) in addition to a PI ice sheet configuration based on BedMap2 (*38*). The full collapse and ice shelf collapse configurations from (*39*) account for ~4 m and ~2 m of sea level rise above PI and the ASE collapse configuration from (*20*) accounts for ~4 m of sea level rise. We use PI ice sheet configurations from each ice sheet model simulation to correct for biases in topography that might be inherent to the ice sheet model. This is accomplished by adding the difference between the modeled PI ice sheet and the modeled LIG ice sheet to the default CESM topography. Each reduced ice sheet configuration results in new exposed ocean where there was previously ice sheet. Resolving these locations as the ice sheet retreats is important for capturing potential vapor sources relevant for Antarctic moisture transport. We use modeled bedrock topography from the ice sheet model data to properly incorporate new bathymetry as the ice sheet retreats and more ocean is exposed. This is done using a similar anomaly method as done for ice sheet topography.

4.3 Hosing experiments

We apply a uniform freshwater forcing across the North Atlantic and Southern Ocean in many of our experiments. The North Atlantic hosing uses 0.2 Sv of freshwater forcing for 1000 years per experiment applied at the surface between 50° and 70°N and 80°W and 20°E excluding the Hudson Bay. The Southern Ocean hosing similarly uses 0.2 Sv of freshwater forcing for 500 years per experiment and is applied uniformly from 60°S poleward. Freshwater uses a $\delta^{18}O$ value of -30‰ and a δD value of -240‰ in both hemispheres. These rates of freshwater forcing are similar to previous hosing experiments using CESM (*54*). The Southern Ocean hosing rate is faster than observed Antarctic melt (*55*) but could be representative of a rapid retreat of the WAIS and should be thought of as a sensitivity test. The North Atlantic hosing is applied for all ice sheet configurations at the LIG to test the sensitivity of regional climate to freshwater forcing likely at the end of Heinrich Event 11 (*29*). The Southern Ocean hosing is applied to each simulation with a reduced WAIS to account for the freshwater released into the Southern Ocean as a result of a collapse. One additional dual hosing experiment applies both the North Atlantic and Southern Ocean freshwater

forcing to the *LIG_collapsed* experiment initialized from the *LIG_collapsed_NAFWF* simulation. This is meant to capture the "most likely" collapse scenario where a North Atlantic meltwater pulse warms the Southern Ocean and causes the rapid retreat of the WAIS.

4.4 Last Interglacial ice core records

There are eight Antarctic water isotopes records measured in ice dating to the LIG discussed in this study. East Antarctic records, including EPICA Dronning Maud Land (EDML), EPICA Dome C (EDC), Vostok, Talos Dome (TALDICE) (*56*), Dome Fuji (DF) (*57*), and Taylor Dome (TD) (*58*) (Fig. S2a), covering a large spatial range of the East Antarctic Ice Sheet. Early in the LIG, $\delta^{18}O$ records are enriched by up to 2-4‰ and this maximum is largely synchronous between records (*25*).

Three additional records from the WAIS (Fig. S2b), Patriot Hills (*19*), Skytrain Ice Rise (*46*), and Mount Moulton (*26, 59*), potentially recording the signals of ice sheet collapse. $\delta^{18}O_{ice}$ values in West Antarctic ice are enriched between 1-5‰ during the LIG. Neither Skytrain Ice Rise nor Patriot Hills contain ice dated to 130-127 ka, the warmest period of the LIG in the Southern Hemisphere. However, the $\delta^{18}O_{ice}$ enrichment recorded in ice cores from both East and West Antarctica early in the LIG is synchronous with elevated global mean sea levels from several reconstructions (*13, 60–62*) (Fig. S2c). This implicates Antarctic change as a potential driver of the LIG sea level highstand but with varying timing and sea level contributions.

4.5 Assessing model $\delta^{18}O$ and ocean surface conditions

To compare ice core $\delta^{18}O_{ice}$ anomalies during the LIG, we use the maximum value of $\delta^{18}O_{ice}$ from between 130 and 126 ka. We consider freshwater flux and changes in ice sheet topography to be dominant local forcings relative to orbital and greenhouse gas forcing, enabling the use of a maximum rather than a strict time slice. For EDC and DF, where there are a large number of data points we use a five point smoothing function to determine the peak $\delta^{18}O_{ice}$. The SIR record lacks $\delta^{18}O$ dated to the early LIG, so we use the average of the earliest 3 data points dating to ~126 ka. Given uncertainties in late-Holocene conditions and the early date of ~132,800 years ago for the Patriot Hills record, we exclude it from our analysis. All other records use the anomaly between the peak LIG value and the last 2,000 years of the Holocene. These are compared to the annually

averaged, precipitation weighted $\delta^{18}O_p$ anomalies between each LIG simulation and our PI control.

For summertime SSTs and September SICs, we use the early LIG SSTs as reported in (*3,4,23,37*). Anomalies are obtained by differencing the peak LIG SSTs and SICs with the average 1850-1900 values from HadISST (*63*) from the nearest grid cells. These are compared with annually averaged, calendar adjusted, summertime ocean temperatures from the upper 50 m, and SICs from our iCESM simulations.

We assess the accuracy of each simulation as the case that minimizes the mean squared error (MSE) and bias (b):

$$MSE = \frac{\Sigma_i^n (X_{model} - X_{core})^2}{n} \tag{1}$$

$$b = \frac{\Sigma_i^n (X_{model} - X_{core})}{n} \tag{2}$$

where X_{model} is the model value and X_{core} is the proxy value. We consider MSE to represent errors that can arise via the common disagreement between model and proxy among different proxy locations and the disagreement in the pattern of our simulated field. Bias (b) is thought the represent the common disagreement between model and proxy data across locations. Here, MSE can be decomposed as $MSE = b^2 + \epsilon$, where ϵ is the variance (*32*).

4.6 Water tag analysis

We run 50 additional years of the *PI*, *LIG*, *LIG_NAFWF*, *LIG_collapsed*, *LIG_collapsed_NAFWF*, and *LIG_collapsed_SOFWF* where evaporative fluxes originating from 10^o latitudinal bins spanning from the Equator to 90°S from the Atlantic, Indian, and Pacific Ocean are tracked from evaporation to precipitation (Methods) (*36, 64*). We use a method inspired by (*65*) to decompose the drivers of $\delta^{18}O_p$ change as: changes in source vapor ($\Delta\delta^{18}O_{v,source}$), changes due to the preferential rainout of heavy isotopologues ($\Delta(\delta^{18}O_{v,AIS} - \delta^{18}O_{v,source})$), and changes due to fractionation during condensation ($\Delta(\delta^{18}O_{p,AIS} - \delta^{18}O_{v,AIS})$).

The change in $\delta^{18}O_v$ at the source region is determined using:

$$\Delta\delta^{18}O_{v,source} = \Sigma_i(\delta^{18}O^{LIG}_{v,source_i} - \delta^{18}O^{PI}_{v,source_i})\frac{P_i}{\Sigma_j P_j} \tag{3}$$

where $\delta^{18}O_{v,source}$ indicates the lowest level vapor at the source region and *i* indicates the *i*th source. By using the lowest level vapor, we assume this is vapor evaporating at a specified source region.

This yields a $\Delta\delta^{18}O_{v,source}$ field for all of the AIS for each experiment. The rainout contribution to $\delta^{18}O$ is calculation with:

$$\Delta\delta^{18}O_{v,AIS} - \Delta\delta^{18}O_{v,source} \tag{4}$$

where

$$\Delta\delta^{18}O_{v,AIS} = \delta^{18}O^{LIG}_{v,AIS} - \delta^{18}O^{PI}_{v,AIS} \tag{5}$$

and $\delta^{18}O_{v,AIS}$ is the column integrated $\delta^{18}O_v$ at the AIS. The condensation contribution is then calculated with:

$$\Delta\delta^{18}O_{p,AIS} - \Delta\delta^{18}O_{v,AIS} \tag{6}$$

where both quantities are anomalies at the LIG compared to the PI. Finally, the mean latitude of moisture source calculates an average latitude of moisture from the fractional precipitation at each grid cell. We sum across basins (Pacific, Atlantic, and Indian Oceans) to obtain latitudinal bins of moisture for each cell. These are converted to fractions of the total precipitation for each point and then multiplied by the mid-point latitude for each bin. The average of this linear combination is used as the mean latitude of moisture sourced for that grid point. Figure 7p,q,r,s,t shows the anomaly between the relevant LIG fields and PI field calculated in this way.

To determine the contribution of the seasonal distribution of precipitation to the annually averaged $\delta^{18}O_p$ signal, we reweigh monthly averaged $\delta^{18}O_p$ from the LIG with the PI precipitation fraction:

$$\Delta\delta^{18}O^{LIG}_{p,PI} = \Delta\frac{\Sigma\delta^{18}O^{LIG}_{p}P^{PI}_{i}}{\Sigma P^{PI}_{i}} \tag{7}$$

where $\delta^{18}O^{LIG}_{p}$ is the monthly averaged $\delta^{18}O_p$ from the LIG and P^{PI}_{i} is the monthly averaged precipitation for the preindustrial. This equation gives us the contribution to the overall $\delta^{18}O_p$ signal that is due to changes in the water isotopic ratio at the LIG, rather than seasonality. To determine the seasonal signal, we instead use the LIG precipitation fraction and the monthly averaged $\delta^{18}O_p$ for the PI giving us the following equation.

$$\Delta\delta^{18}O^{PI}_{p,LIG} = \Delta\frac{\Sigma\delta^{18}O^{PI}_{p}P^{LIG}_{i}}{\Sigma P^{LIG}_{i}} \tag{8}$$

This yields the contribution to the annual average $\delta^{18}O_p$ signal that is purely due to seasonal changes.

Table 1: **Table of simulations used the characterize the topographic and meltwater impact on Antarctic $\delta^{18}O_{ice}$ and Southern Ocean surface conditions.**

Alias	Timeslice	Antarctic Ice Sheet Configuration	Freshwater forcing
PI	PI	PI	-
LIG	LIG	PI	-
LIG_NAFWF	LIG	PI	NAFWF[1]
LIG_noASE	LIG	noASE[3]	-
LIG_noASE_NAFWF	LIG	noASE	SOFWF[2]
LIG_noASE_SOFWF	LIG	noASE	SOFWF
LIG_noShelves	LIG	noShelves[4]	-
LIG_noShelves_NAFWF	LIG	noShelves	NAFWF
LIG_noShelves_SOFWF	LIG	noShelves	SOFWF
LIG_collapsed	LIG	collapsed[4]	-
LIG_collapsed_NAFWF	LIG	collapsed	NAFWF
LIG_collapsed_SOFWF	LIG	collapsed	SOFWF
LIG_collapsed_NAFWF_SOFWF	LIG	collapsed	NAFWF + SOFWF [5]

[1] NAFWF: 0.2 Sv North Atlantic 1000 years.

[2] SOFWF: 0.2 Sv Southern Ocean 500 years.

[3] Based on simulations from (*20*).

[4] Based on simulations from (*39*).

[5] Simulation is branched from the end of *LIG_collapsed_NAFWF* and run for 500 years with additional Southern Ocean freshwater forcing.

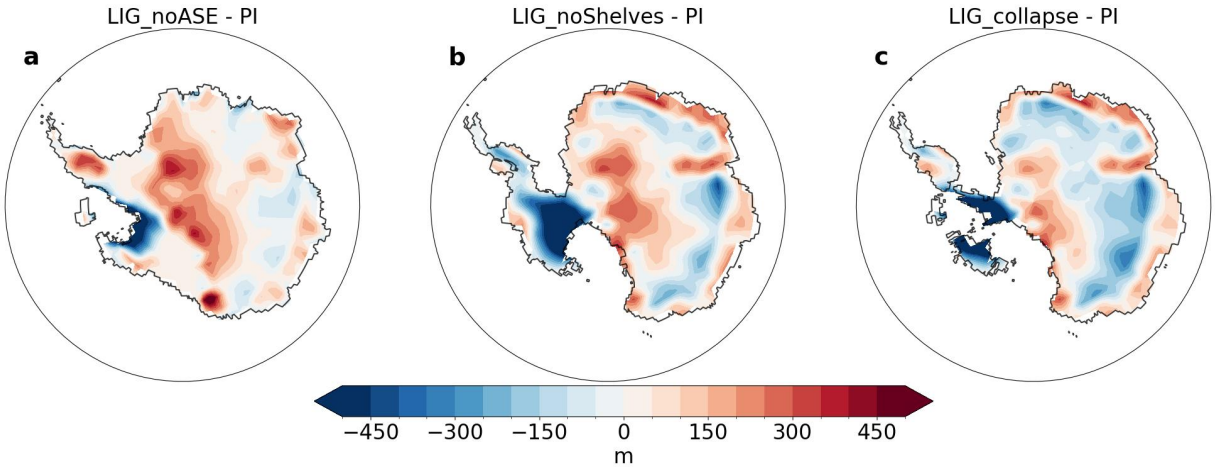


Figure 1: **Elevation anomalies between Last Interglacial ice sheet configurations and the preindustrial**. **a** Amundsen Sea Embayment collapse (*LIG_noASE*) configuration, **b** Ross and Ronne-Filchner ice shelf collapse (*LIG_noShelves*) configuration, and **c** complete collapse (*LIG_collapse*) configuration.

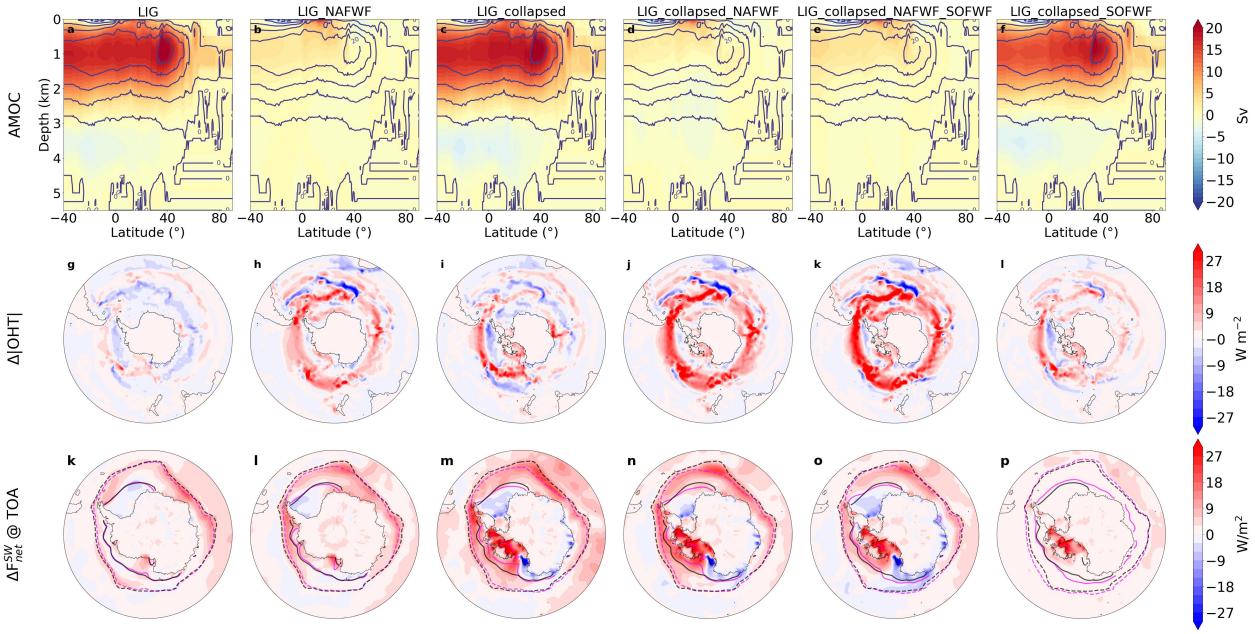


Figure 2: **Large-scale ocean response to glacial meltwater in the North Atlantic or Southern Ocean and WAIS collapse. a-f**, Atlantic Meridional Overturning Circulation (AMOC) anomalies for each LIG simulation with respect to the PI. PI AMOC is shown in purple contours. **g-l**, lateral ocean heat transport anomalies between the LIG and PI. **k-p**, top-of-atmosphere (TAO) shortwave (SW) radiative imbalance between the LIG and PI. The September 30% sea ice concentration contour shown for PI (black dashed), LIG (pink dashed), and the march PI March 30% sea ice concentration contour for PI (black solid), and LIG March (pink solid).

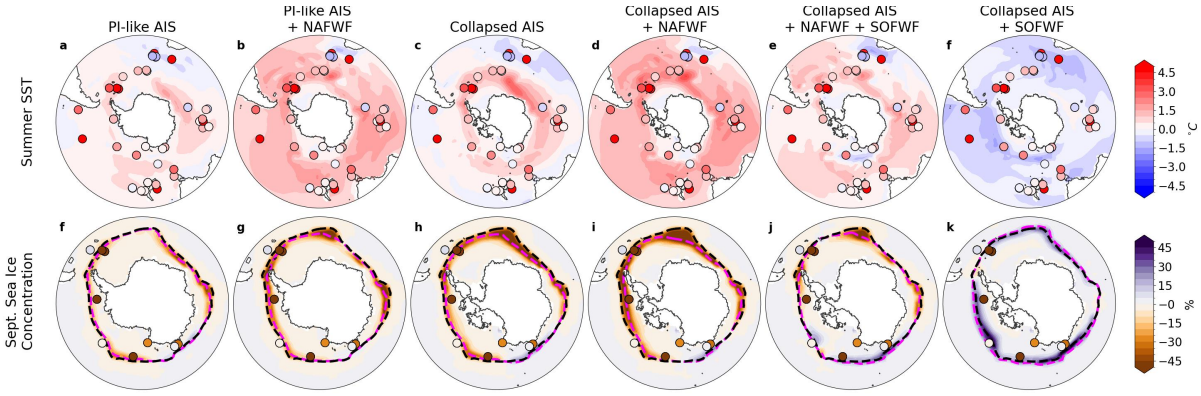


Figure 3: **Austral summer sea surface temperature and September sea ice concentration anomalies between the LIG and PI**. **a,f** PI-like Antarctic ice sheet, **b,g** PI-like Antarctic ice sheet with North Atlantic hosing, **c,h** fully collapsed Antarctic ice sheet, **d,i** fully collapsed Antarctic ice sheet with North Atlantic hosing, **e,j** fully collapsed Antarctic ice sheet with North Atlantic and Southern Ocean hosing, and **f,k** fully collapsed Antarctic ice sheet with Southern Ocean hosing. Filled circles show proxy reconstructed temperature anomalies from (*3, 4, 23, 37*). Black and pink contours in **f-k** show the 30% September sea ice concentration contour for the PI and LIG, respectively.

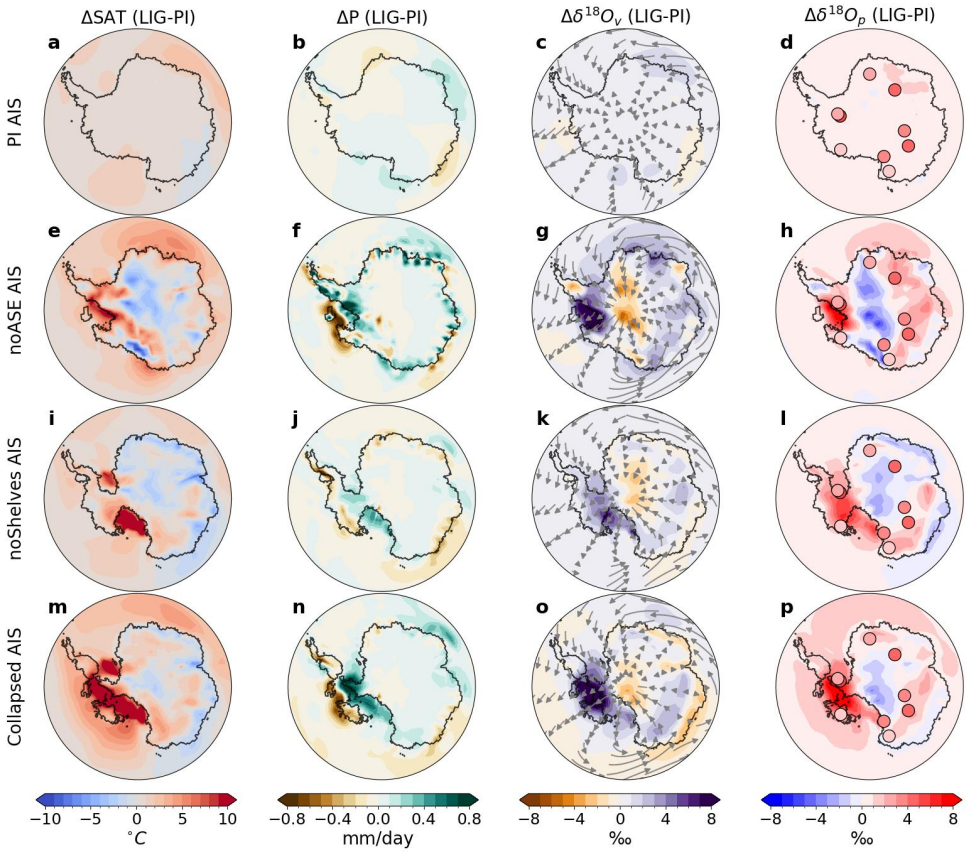


Figure 4: **Impact of elevation on surface temperature, precipitation, $\delta^{18}O_v$, and $\delta^{18}O_p$. a,e,i,m**, Surface temperature anomalies (ΔSAT) between the LIG and the PI with a **a** PI-like, **e** collapsed Amundsen Sea Embayment (ASE), **i** collapsed Ross and Filchner-Ronne ice shelves (noShelves), and **m** completely collapsed (collapsed) Antarctic ice sheet configuration. **b,f,j,n**, as in **a,e,i,m** but for anomalies in precipitation (ΔP). **c,g,k,o**, as in **a,e,i,m** but for anomalies in the average $\delta^{18}O$ of vapor ($\delta^{18}O_v$) with 500 hPa winds for each LIG climate (vectors). **d,h,l,p**, as in **a,e,i,m** but for anomalies in $\delta^{18}O$ or precipitation ($\delta^{18}O_p$) with ice core data plotted (*19, 25, 26, 46, 58*).

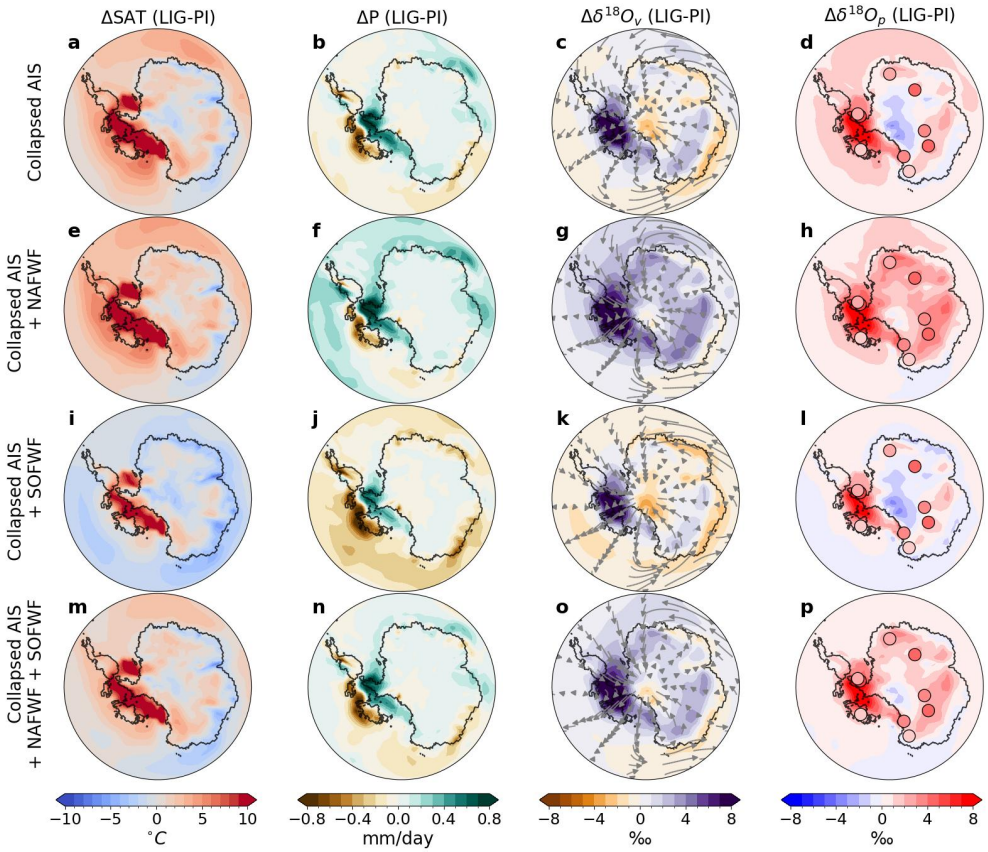


Figure 5: **Impact of freshwater flux on surface temperature, precipitation,** $\delta^{18}O_v$**, and** $\delta^{18}O_p$ **with a fully collapsed West Antarctic Ice Sheet. a,e,i,m**, ΔSAT anomalies between the LIG and the PI with **a** no freshwater flux, **e** North Atlantic freshwater flux (NAFWF), **i** Southern Ocean freshwater flux (SOFWF), and **m** simultaneous North Atlantic and Southern Ocean freshwater flux (NAFWF + SOFWF). **b,f,j,n**, as in **a,e,i,m** but for anomalies in precipitation (ΔP). **c,g,k,o**, as in **a,e,i,m** but for anomalies in the $\delta^{18}O$ of vapor ($\delta^{18}O_v$) with 500 hPa winds for each LIG climate (vectors). **d,h,l,p**, as in **a,e,i,m** but for anomalies in the $\delta^{18}O$ of precipitation ($\delta^{18}O_p$) with ice core data plotted (*19, 25, 26, 46, 58*).

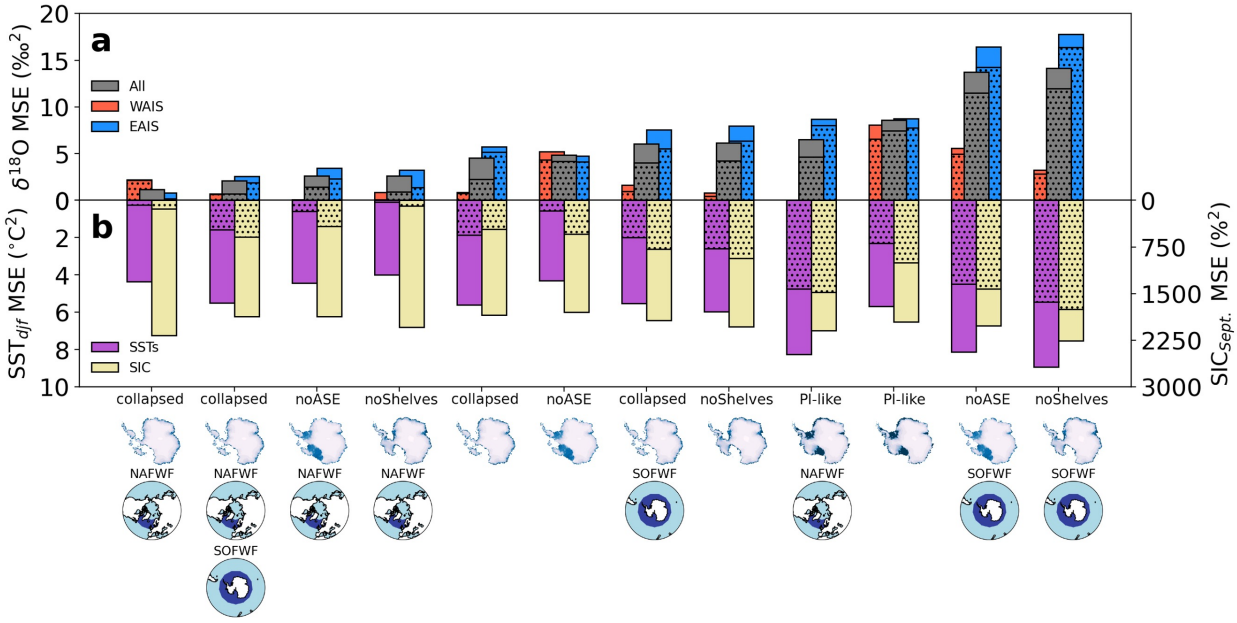


Figure 6: **Statistical comparison between modeled and observed $\delta^{18}O$, SST$_{djf}$, and September SICs. a**, Mean squared error (MSE) between ice core $\delta^{18}O$ and modeled $\delta^{18}O$ for 6 East Antarctic ice cores (blue) (*25, 58*) and 2 West Antarctic ice cores (red) (*19, 26, 46, 59*) (all cores; grey). **b**, MSE between summertime (DJF) SSTs (SST$_{djf}$) (*4, 23, 37*) (pink) and September sea ice concentrations (*3*) (taupe) proxies and model results. Stippling indicates the squared bias (*b*) error for each simulation.

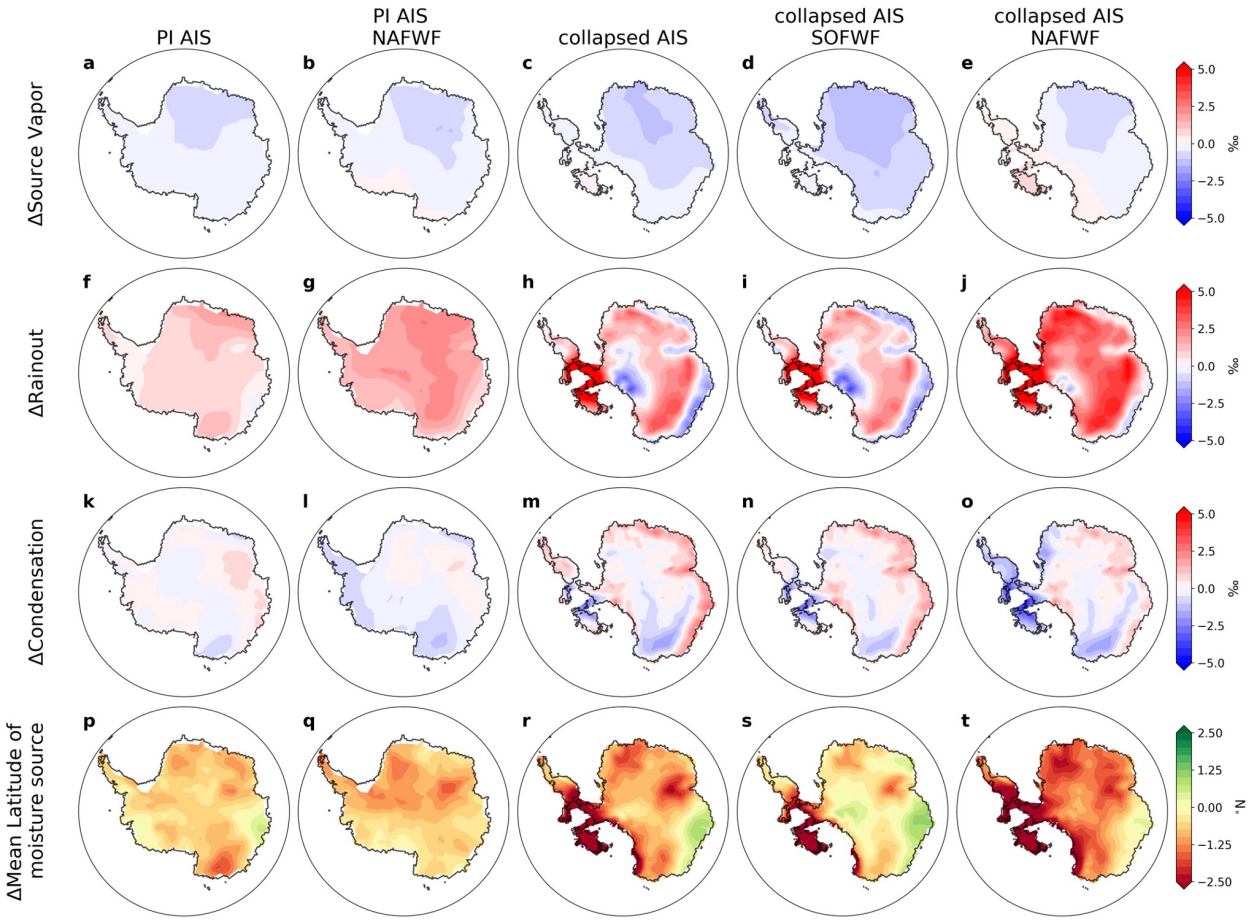


Figure 7: **Drivers of $\delta^{18}O$ as found through water tag analysis. a-e**, anomaly between LIG and PI $\delta^{18}O_v$ at the weighted source regions for each point in space for **a** a PI-like AIS, **b** a PI-like AIS with NAFWF, **c** a collapsed AIS, **d** a collapsed AIS with SOFWF, and **e** a collapsed AIS with NAFWF. **f-j**, as in **a-e** for the difference between $\delta^{18}O_v$ at the AIS ($\delta^{18}O_{v,AIS}$) and $\delta^{18}O_v$ at the weighted source regions ($\delta^{18}O_{v,source}$). **k-o**, as in **a-e** for the difference between $\delta^{18}O_p$ at the AIS and $\delta^{18}O_v$ at the AIS. **p-t**, as in **a-e** showing the weighted mean latitude of source vapor making up the precipitation at each point over the AIS.

References and Notes

1. J. S. Hoffman, P. U. Clark, A. C. Parnell, F. He, Regional and global sea-surface temperatures during the last interglaciation. *Science* **355** (6322), 276–279 (2017).

2. F. Vermassen, *et al.*, A seasonally ice-free Arctic Ocean during the Last Interglacial. *Nature Geoscience* **16** (8), 723–729 (2023).

3. M. Chadwick, X. Crosta, O. Esper, L. Thöle, K. E. Kohfeld, Compilation of Southern Ocean sea-ice records covering the last glacial-interglacial cycle (12–130 ka). *Climate of the Past* **18** (8), 1815–1829 (2022).

4. M.-V. Guarino, *et al.*, Sea-ice-free Arctic during the Last Interglacial supports fast future loss. *Nature Climate Change* **10** (10), 928–932 (2020).

5. D. R. Muhs, T. A. Ager, J. E. Begét, Vegetation and paleoclimate of the last interglacial period, central Alaska. *Quaternary Science Reviews* **20** (1-3), 41–61 (2001).

6. F. S. Pausata, *et al.*, The greening of the Sahara: Past changes and future implications. *One Earth* **2** (3), 235–250 (2020).

7. B. L. Otto-Bliesner, *et al.*, Large-scale features of Last Interglacial climate: Results from evaluating the lig127k simulations for CMIP6-PMIP4. *Climate of the Past Discussions* **2020**, 1–41 (2020).

8. IPCC, *Climate Change 2021: The Physical Science Basis. Contribution of Working Group I to the Sixth Assessment Report of the Intergovernmental Panel on Climate Change* (Cambridge University Press, Cambridge, UK and New York, NY, USA) (2021), doi:10.1017/9781009157896, `https://report.ipcc.ch/ar6/wg1/IPCC_AR6_WGI_FullReport.pdf`.

9. K. Vyverberg, *et al.*, Episodic reef growth in the Last Interglacial driven by competing influence of polar ice sheets to sea level rise. *Science Advances* **11** (24), eadu3701 (2025), doi:10.1126/sciadv.adu3701.

10. N. P. McKay, J. T. Overpeck, B. L. Otto-Bliesner, The role of ocean thermal expansion in Last Interglacial sea level rise. *Geophysical Research Letters* **38** (14) (2011).

11. V. Radić, R. Hock, Regionally differentiated contribution of mountain glaciers and ice caps to future sea-level rise. *Nature Geoscience* **4** (2), 91–94 (2011).

12. A. Dutton, *et al.*, Sea-level rise due to polar ice-sheet mass loss during past warm periods. *science* **349** (6244), aaa4019 (2015).

13. E. J. Rohling, *et al.*, Asynchronous Antarctic and Greenland ice-volume contributions to the last interglacial sea-level highstand. *Nature Communications* **10** (1), 5040 (2019).

14. R. C. Creel, J. Austermann, Glacial isostatic adjustment driven by asymmetric ice sheet melt during the Last Interglacial causes multiple local sea-level peaks. *Geology* **53** (3), 253–258 (2025).

15. P. U. Clark, *et al.*, Oceanic forcing of penultimate deglacial and last interglacial sea-level rise. *Nature* **577** (7792), 660–664 (2020).

16. R. P. Scherer, *et al.*, Pleistocene collapse of the West Antarctic ice sheet. *Science* **281** (5373), 82–85 (1998).

17. S. C. Lau, *et al.*, Genomic evidence for West Antarctic ice sheet collapse during the last interglacial. *Science* **382** (6677), 1384–1389 (2023).

18. A. E. Carlson, B. L. Beard, R. G. Hatfield, M. Laffin, Absence of West Antarctic-sourced silt at ODP Site 1096 in the Bellingshausen Sea during the last interglaciation: Support for West Antarctic ice-sheet deglaciation. *Quaternary Science Reviews* **261**, 106939 (2021).

19. C. S. Turney, *et al.*, Early Last Interglacial ocean warming drove substantial ice mass loss from Antarctica. *Proceedings of the National Academy of Sciences* **117** (8), 3996–4006 (2020).

20. N. R. Golledge, *et al.*, Retreat of the Antarctic Ice Sheet during the Last Interglaciation and implications for future change. *Geophysical Research Letters* **48** (17), e2021GL094513 (2021).

21. J. Sutter, P. Gierz, K. Grosfeld, M. Thoma, G. Lohmann, Ocean temperature thresholds for last interglacial West Antarctic Ice Sheet collapse. *Geophysical Research Letters* **43** (6), 2675–2682 (2016).

22. R. M. DeConto, D. Pollard, Contribution of Antarctica to past and future sea-level rise. *Nature* **531** (7596), 591–597 (2016).

23. D. M. Chandler, *et al.*, Antarctic Ice Sheet tipping in the last 800,000 years warns of future ice loss. *Communications Earth & Environment* **6** (1), 420 (2025).

24. N. R. Golledge, *et al.*, The multi-millennial Antarctic commitment to future sea-level rise. *Nature* **526** (7573), 421–425 (2015).

25. V. Masson-Delmotte, *et al.*, A comparison of the present and last interglacial periods in six Antarctic ice cores. *Climate of the Past* **7** (2), 397–423 (2011), doi:10.5194/cp-7-397-2011, https://cp.copernicus.org/articles/7/397/2011/.

26. E. J. Steig, *et al.*, Influence of West Antarctic ice sheet collapse on Antarctic surface climate. *Geophysical Research Letters* **42** (12), 4862–4868 (2015).

27. P. Holden, *et al.*, Interhemispheric coupling, the West Antarctic ice sheet and warm Antarctic interglacials. *Climate of the Past* **6** (4), 431–443 (2010).

28. M. D. Holloway, *et al.*, Antarctic last interglacial isotope peak in response to sea ice retreat not ice-sheet collapse. *Nature communications* **7** (1), 12293 (2016).

29. G. Marino, *et al.*, Bipolar seesaw control on last interglacial sea level. *Nature* **522** (7555), 197–201 (2015).

30. M. Dütsch, E. J. Steig, P. N. Blossey, A. G. Pauling, Response of water isotopes in precipitation to a collapse of the West Antarctic Ice Sheet in high-resolution simulations with the weather research and forecasting model. *Journal of Climate* **36** (16), 5417–5430 (2023).

31. D. K. Hutchinson, L. Menviel, K. J. Meissner, A. M. Hogg, East Antarctic warming forced by ice loss during the Last Interglacial. *Nature Communications* **15** (1), 1026 (2024).

32. H. Zou, L. C. Sime, N. A. Bertler, E. D. Keller, E. W. Wolff, Plausible last interglacial Antarctic Ice Sheet changes do not fully explain antarctic ice core water isotope records. *Geophysical Research Letters* **52** (1), e2024GL110657 (2025).

33. M. D. Holloway, L. C. Sime, J. S. Singarayer, J. C. Tindall, P. J. Valdes, Simulating the 128-ka Antarctic climate response to northern hemisphere ice sheet melting using the isotope-enabled HadCM3. *Geophysical Research Letters* **45** (21), 11–921 (2018).

34. Q. Gao, *et al.*, Assessment of the southern polar and subpolar warming in the PMIP4 Last Interglacial simulations using paleoclimate data syntheses. *Climate of the Past* **21** (2), 419–440 (2025).

35. L. C. Sime, *et al.*, H11 meltwater and standard 127 ka Last Interglacial simulations suggest more modest peak temperatures for both Greenland and Antarctica: a multi-model study of water isotopes. *Climate of the Past* **21** (10), 1725–1753 (2025).

36. E. Brady, *et al.*, The connected isotopic water cycle in the Community Earth System Model version 1. *Journal of Advances in Modeling Earth Systems* **11** (8), 2547–2566 (2019).

37. M. Chadwick, L. Sime, C. Allen, M.-V. Guarino, Model-data comparison of Antarctic winter sea-ice extent and Southern Ocean sea-surface temperatures during Marine Isotope Stage 5e. *Paleoceanography and Paleoclimatology* **38** (6), e2022PA004600 (2023).

38. P. Fretwell, *et al.*, Bedmap2: improved ice bed, surface and thickness datasets for Antarctica. *The cryosphere* **7** (1), 375–393 (2013).

39. J. Sutter, *et al.*, Modelling the Antarctic Ice Sheet across the mid-Pleistocene transition–implications for Oldest Ice. *The Cryosphere* **13** (7), 2023–2041 (2019).

40. M. Berdahl, *et al.*, Antarctic climate response in Last Interglacial simulations using the Community Earth System Model (CESM2). *Climate of the Past* **20** (10), 2349–2371 (2024).

41. R. Diamond, *et al.*, A weakened AMOC could cause Southern Ocean temperature and sea-ice change on multidecadal timescales. *Journal of Geophysical Research: Oceans* **130** (7), e2024JC022027 (2025).

42. A. G. Pauling, C. M. Bitz, E. J. Steig, Linearity of the climate system response to raising and lowering West Antarctic and coastal Antarctic topography. *Journal of Climate* **36** (18), 6195–6212 (2023).

43. H. K. Singh, C. M. Bitz, D. M. Frierson, The global climate response to lowering surface orography of Antarctica and the importance of atmosphere–ocean coupling. *Journal of Climate* **29** (11), 4137–4153 (2016).

44. I. James, On the forcing of planetary-scale Rossby waves by Antarctica. *Quarterly Journal of the Royal Meteorological Society* **114** (481), 619–637 (1988).

45. E. Capron, A. Govin, R. Feng, B. L. Otto-Bliesner, E. Wolff, Critical evaluation of climate syntheses to benchmark CMIP6/PMIP4 127 ka Last Interglacial simulations in the high-latitude regions. *Quaternary Science Reviews* **168**, 137–150 (2017).

46. E. W. Wolff, *et al.*, The Ronne Ice Shelf survived the last interglacial. *Nature* **638** (8049), 133–137 (2025).

47. M. Casado, *et al.*, Water isotope–temperature relationship variability across Antarctica set by atmospheric circulation. *Nature Geoscience* pp. 1–8 (2026).

48. Y. Yan, *et al.*, Enhanced moisture delivery into Victoria Land, East Antarctica, during the early Last Interglacial: implications for West Antarctic Ice Sheet stability. *Climate of the Past* **17** (5), 1841–1855 (2021).

49. A. J. Carter, *et al.*, Diminished Ross Ice Shelf and West Antarctic Ice Sheet during Last Interglacial warming. *Nature Geoscience* pp. 1–8 (2026).

50. M. Werner, J. Jouzel, V. Masson-Delmotte, G. Lohmann, Reconciling glacial Antarctic water stable isotopes with ice sheet topography and the isotopic paleothermometer. *Nature communications* **9** (1), 3537 (2018).

51. N. K.-H. Yeung, *et al.*, Last Interglacial subsurface warming on the Antarctic shelf triggered by reduced deep-ocean convection. *Communications Earth & Environment* **5** (1), 212 (2024).

52. W. Cai, *et al.*, Southern Ocean warming and its climatic impacts. *Science Bulletin* **68** (9), 946–960 (2023).

53. B. L. Otto-Bliesner, *et al.*, Large-scale features of Last Interglacial climate: results from evaluating the lig127k simulations for the Coupled Model Intercomparison Project (CMIP6)–Paleoclimate Modeling Intercomparison Project (PMIP4). *Climate of the Past* **17** (1), 63–94 (2021).

54. C. He, *et al.*, Abrupt Heinrich Stadial 1 cooling missing in Greenland oxygen isotopes. *Science advances* **7** (25), eabh1007 (2021).

55. M. A. Depoorter, *et al.*, Calving fluxes and basal melt rates of Antarctic ice shelves. *Nature* **502** (7469), 89–92 (2013).

56. L. Bazin, *et al.*, The Antarctic ice core chronology (AICC2012) (2013), doi:10.1594/PANGAEA.824894, `https://doi.org/10.1594/PANGAEA.824894`.

57. R. Uemura, *et al.*, Asynchrony between Antarctic temperature and CO2 associated with obliquity over the past 720,000 years. *Nature communications* **9** (1), 961 (2018).

58. E. J. Steig, *et al.*, Wisconsinan and Holocene climate history from an ice core at Taylor Dome, western Ross Embayment, Antarctica. *Geografiska Annaler: Series A, Physical Geography* **82** (2–3), 213–235 (2000), doi:10.1111/j.0435-3676.2000.00122.x.

59. E. V. Korotkikh, *et al.*, The last interglacial as represented in the glaciochemical record from Mount Moulton Blue Ice Area, West Antarctica. *Quaternary Science Reviews* **30** (15-16), 1940–1947 (2011).

60. K. Grant, *et al.*, Rapid coupling between ice volume and polar temperature over the past 150,000 years. *Nature* **491** (7426), 744–747 (2012).

61. R. E. Kopp, F. J. Simons, J. X. Mitrovica, A. C. Maloof, M. Oppenheimer, Probabilistic assessment of sea level during the last interglacial stage. *Nature* **462** (7275), 863–867 (2009).

62. R. L. Barnett, *et al.*, Constraining the contribution of the Antarctic Ice Sheet to Last Interglacial sea level. *Science advances* **9** (27), eadf0198 (2023).

63. N. A. Rayner, *et al.*, Global analyses of sea surface temperature, sea ice, and night marine air temperature since the late nineteenth century. *Journal of Geophysical Research: Atmospheres* **108** (D14) (2003).

64. P. B. Goddard, C. R. Tabor, T. R. Jones, Utilizing ice core and climate model data to understand seasonal west Antarctic variability. *Journal of Climate* **34** (24), 10007–10026 (2021).

65. C. R. Tabor, *et al.*, Interpreting precession-driven δ18O variability in the South Asian monsoon region. *Journal of Geophysical Research: Atmospheres* **123** (11), 5927–5946 (2018).

Acknowledgments

We acknowledge the computing resources and support provided by the National Center for Atmospheric Research (NCAR) which is sponsored by the National Science Foundation (NSF). These simulations were completed on the NSF Derecho supercomputer, which is supported by the Computational and Information Systems Laboratory (CISL) at NCAR.

Funding: This study was funded by National Science Foundation (NSF) OPP-2035637 awarded to C.T. The CESM project is primarily supported by the NSF.

Author contributions: Conceptualization: J.Sc., C.T., and S.A. Methodology: J.Sc., C.T., N.G., J.Su., E.S., and R.F. Visualization: J.Sc. Supervision: C.T.. Writing—original draft: J.Sc. and C.T. Writing—review and editing: J.Sc., C.T., R.F., N.G., J.Su., A.C., S.A., and E.S.

Competing interests: The authors declare that they have no competing interests.

Data and materials availability: All data needed to evaluate the conclusions in the paper are present in the paper and/or the Supplementary Materials. Processed model outputs reported in this study are available on Zenodo at https://doi.org/10.5281/zenodo.20939114. Additional model outputs are available from the authors upon request.

Supplementary materials

Figs. S1 to S3

Supplementary Materials for

West Antarctic Ice Sheet collapse and North Atlantic meltwater reconcile Last Interglacial climate records

Joseph Schnaubelt*, Clay Tabor, Ran Feng, Austin Carter, Sarah Aarons, Johannes Sutter, Nicholas Golledge, Eric Steig,

*Corresponding author. Email: joseph.schnaubelt@uconn.edu

This PDF file includes:

Figures S1 to S6

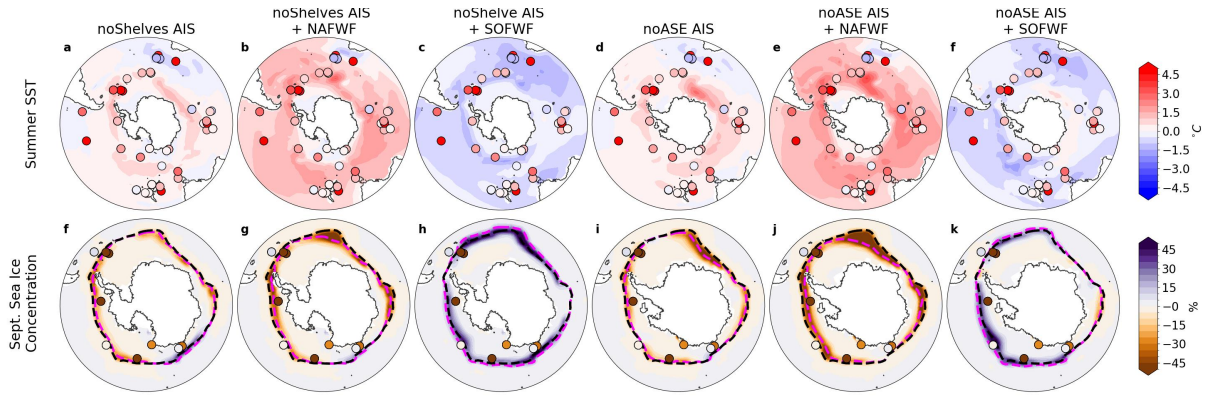


Figure S1: **Summertime SSTs and September sea ice concetrations for the *LIG_noShelves* and *LIG_noASE* simulations.** Same as Figure 2, but for the *LIG_noShelves* AIS configuration **a-c;g-i** and the *LIG_noASE* AIS configuration **d-f;j-l**

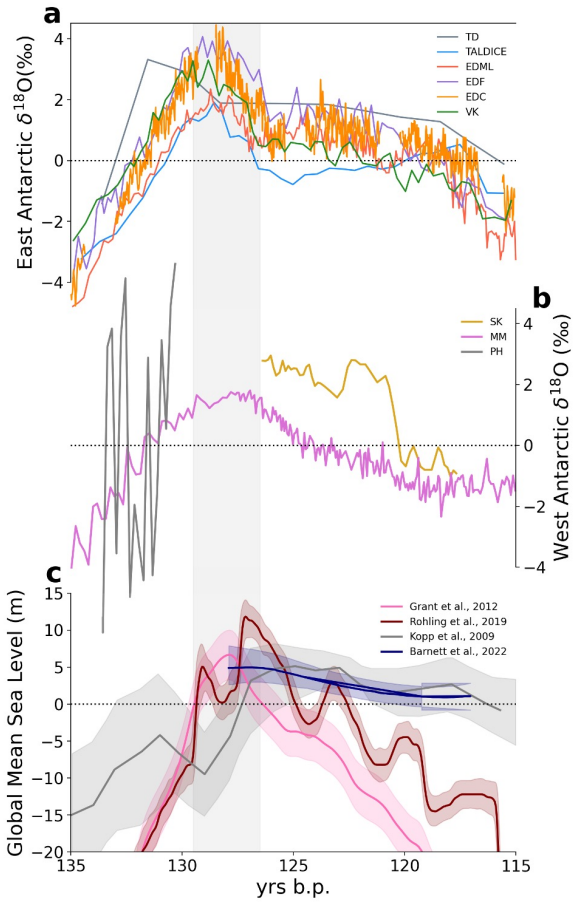


Figure S2: **Antarctic ice core $\delta^{18}O$ and global mean sea level reconstructions over the Penultimate Deglaciation and Last Interglacial. a**, East Antarctic ice core $\delta^{18}O$ anomaly relative to the late Holocene. **b**, West Antarctic ice core $\delta^{18}O$ anomaly relative to the late Holocene. **c**, global mean sea level reconstructions relative to present day sea level.

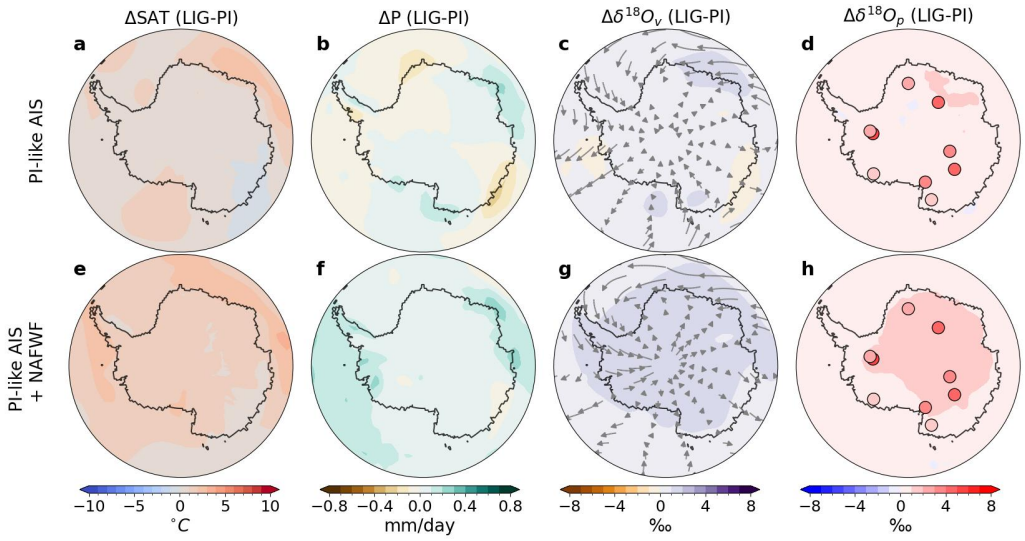


Figure S3: **Antarctic surface conditions at the LIG with a PI-like AIS with and without NAFWF** Same as Figure 4, but for the PI-like AIS configuration **a-d** and the PI-like AIS configuration with NAFWF **e-h**.

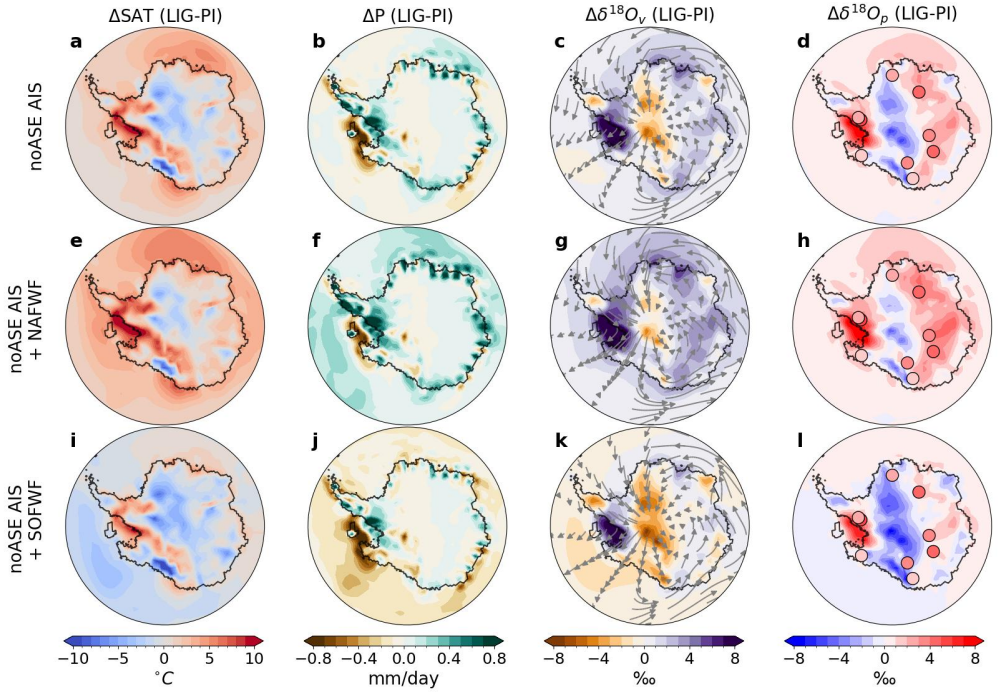


Figure S4: **Antarctic surface conditions at the LIG with a *LIG_noASE* AIS with various freshwater hosing configurations.** Same as Figure 4, but for the *LIG_noASE* AIS configuration **a-d**, the *LIG_noASE* AIS configuration with NAFWF **e-h**, and the *LIG_noASE* AIS configuration with SOFWF **i-l**.

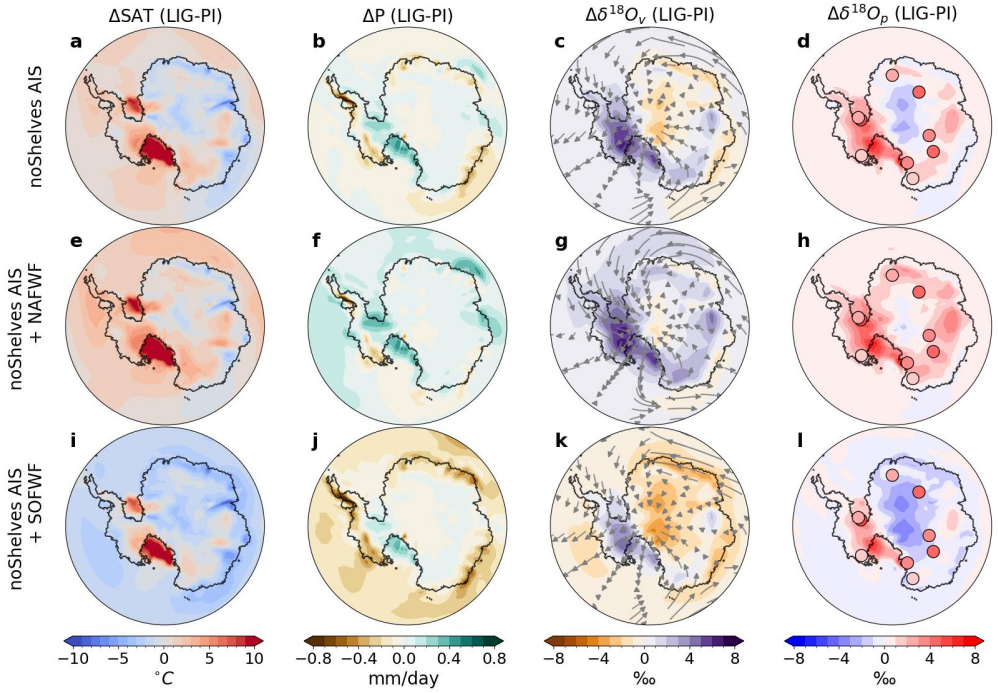


Figure S5: **Antarctic surface conditions at the LIG with a *LIG_noShelves* AIS with various freshwater hosing configurations.** Same as Figure 4, but for the *LIG_noShelves* AIS configuration **a-d**, the *LIG_noShelves* AIS configuration with NAFWF **e-h**, and the *LIG_noShelves* AIS configuration with SOFWF **i-l**.

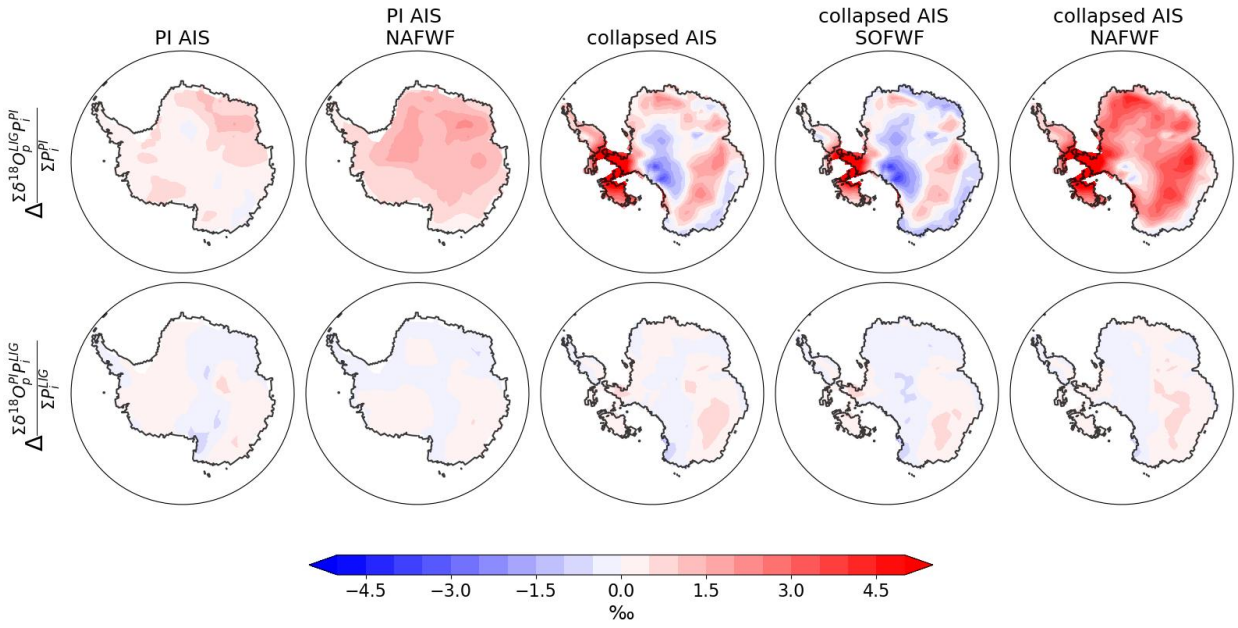


Figure S6: **Decomposition of the impact of seasonal precipitation on Antarctic $\delta^{18}O_p$ with a variety of AIS topographies and freshwater hosing scenarios** Anomalies between the LIG and PI following the same order as Figure 7. **Top** shows the $\delta^{18}O_p$ for the LIG for each case reweighted by the monthly precipitation for the PI. **Bottom** shows the $\delta^{18}O_p$ for the PI reweighted by the monthly precipitation for the LIG.

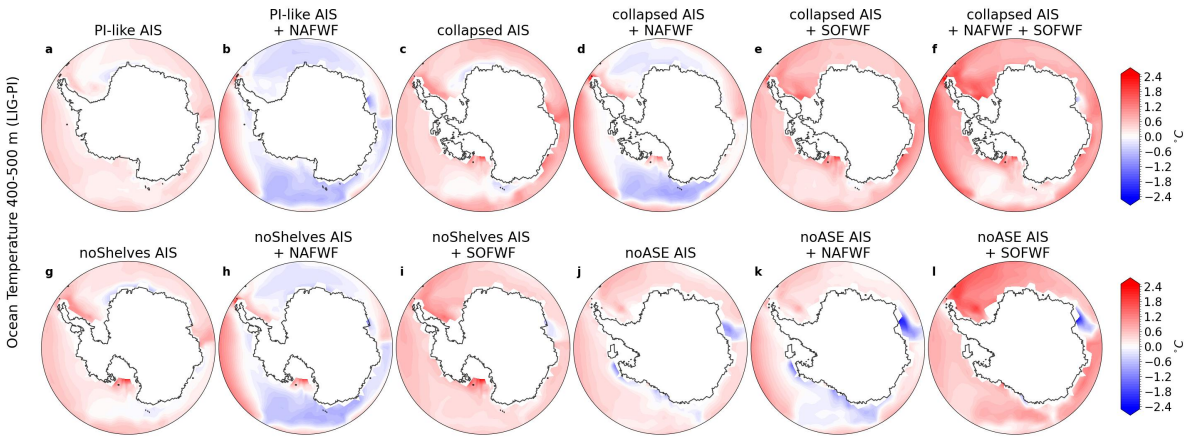


Figure S7: **Subsurface (400-500 m) warming response for each ice sheet and freshwater configurations.**Anomaly between LIG and PI ocean temperature averaged between 400-500 m for the LIG with **a** a PI-like AIS, **b** a PI-like AIS and NAFWF, **c** a fully collapsed WAIS, **d** a fully collapsed WAIS and NAFWF, **e** a fully collapsed WAIS and SOFWF, **f** a fully collapsed WAIS, NAFWF, and SOFWF, **g** the *noShelves* AIS, **h** the *noShelves* AIS and NAFWF, **i** the *noShelves* AIS and SOFWF, **j** the *noASE* AIS, **k** the *noASE* AIS and NAFWF, and finally **l** the *noASE* AIS with SOFWF.